THE JOURNAL OF PHYSICAL CHEMISTRY B

Article

Molecular Dynamics Simulations of a Hyperbranched Poly(ester amide): Statics, Dynamics, and Hydrogen Bonding

I. Tanis, D. Tragoudaras, K. Karatasos, and S. H. Anastasiadis

J. Phys. Chem. B, **2009**, 113 (16), 5356-5368• DOI: 10.1021/jp8097999 • Publication Date (Web): 30 March 2009

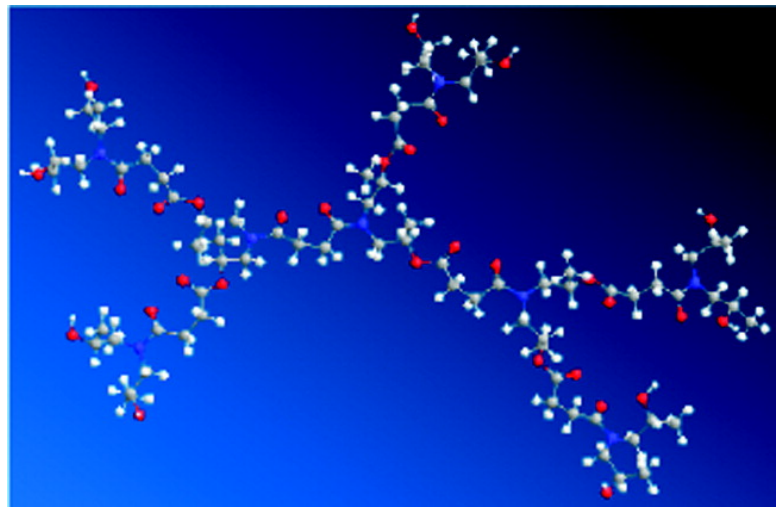

Molecular Dynamics Simulations of a Hyperbranched Poly(ester amide): Statics, Dynamics, and Hydrogen Bonding

I. Tanis,[†] D. Tragoudaras,[†] K. Karatasos,*[,†] and S. H. Anastasiadis[†,‡,§]

Department of Chemical Engineering, Aristotle University of Thessaloniki, 541 24 Thessaloniki, Greece, Institute of Electronic Structure and Laser, Foundation for Research and Technology-Hellas, 711 10 Heraklion, Crete, Greece, and Department of Chemistry, University of Crete, 710 03 Heraklion, Crete, Greece

Received: November 6, 2008; Revised Manuscript Received: January 19, 2009

Fully atomistic molecular dynamics simulations are employed in order to examine static and dynamic characteristics of a hyperbranched poly(ester amide), Hybrane, in the bulk state. The force field used is validated via a comparison to available static, dynamic, and thermodynamic data. Properties pertinent to both local and global length scales like atomic and molecular spatial arrangement, bond-reorientation dynamics, shape and size fluctuations, rotational motion of the whole molecule, and diffusional motion are examined in detail in order to assess the relation between microscopic mechanisms and macroscopic behavior. The atomistic-level detail of the model utilized allows a close examination of the intra- and intermolecular hydrogen-bonding formation and the relevant residence time scales; these are among the key factors that determine the behavior of such polymers in the nanoscale, important for a wide range of applications. The detailed nature of the present investigation will provide insight in a more general basis for the behavior of nonregularly branched polymers of comparable molecular weight and similar chemical composition.

Introduction

Hyperbranched polymers have emerged during the recent years as a promising class of versatile materials for a broad range of novel nanoscale applications.[1,2] Their multiple functionality combined with their suitable nanosized dimensions and their cost-effective synthesis procedures, as compared to dendrimers, suffice to classify them as particularly suitable candidates for applications where up to now expensive regularly branched dendritic molecules had been utilized.[3−6] A particular class of hyperbranched molecules, which belong to the poly(ester amide) family,[7,8] are now produced on an industrial scale at a very competitive cost bearing the commercial name Hybrane.[9] These molecules are already being utilized as key components in several high-added-value applications (e.g., in nanolithography,[10−12] as dispersion agents,[13] surface modifiers,[14] etc.) while they appear as promising candidates for cost-effective pharmaceutical (e.g., drug delivery[15]) formulations. However, despite their great industrial importance, only a few experimental studies have addressed issues related to their detailed characterization and their structure−properties relationships.[8,9,16] On these accounts, a more profound understanding based on a molecular-level picture, regarding the microscopic mechanisms responsible for the manifestation of their macroscopic properties, is highly desirable.

Computer simulations constitute a key tool that can provide information at any level of detail required, particularly when performed in a fully atomistic level. Along these lines, we have performed atomistically detailed molecular dynamics (MD) simulations in order to examine for the first time the behavior of a water-soluble and biocompatible poly(ester amide) molecule (Figure 1) in the melt by means of molecular dynamics simulations, thereby examining certain characteristic static and dynamic properties over different length and time scales. In addition, particular attention has been paid to the study of the formation and the residence time of intra- and intermolecular hydrogen-bonding pairs, because of their significance in mechanisms related for instance to the formation of hydrogen-bond-driven physical polymeric networks,[17] to the solubilization behavior of hydrogen-bonded systems,[18,19] and to the potential of forming hydrogen-bonding-mediated noncovalent complexes with other moieties.[19−21]

Simulation Details

Melt samples comprising 40 Hybrane molecules in fully atomistic representations were constructed by the aid of the Amorphous Cell algorithm.[22] The AMBER force field[23] was employed for the construction of the models and throughout all the other stages of the simulation. This force field has been successfully utilized in analogous simulations of other hyperbranched systems,[24,25] and it accounts for both bonded (bond stretching, angle bending, torsional rotation) and nonbonded interactions (van der Waals, Coulombic). Partial charges were assigned according to the Gasteiger method[26] while all electrostatic interactions between them were calculated via full Ewald summation.[27] The non-Coulombic nonbonded interactions were modeled via a 12-6 Lennard-Jones potential (with a cutoff radius of 10 Å) while for interactions between hydrogen bond donors and acceptors (hydroxyl oxygen, hydroxyl hydrogen, carbonyl oxygen) a 12-10 potential was employed.[28]

The adopted simulation protocol involved the creation of the starting melt configuration at an elevated temperature and successive molecular dynamics cooling steps of 50 K every time under conditions of constant pressure ($P = 1$ atm) and temperature (NPT ensemble). The systems spent several hundred picoseconds (in 1 fs steps) at each cooling step, depending on the temperature (the lower the temperature the longer the NPT

* To whom correspondence should be addressed.
[†] Aristotle University of Thessaloniki.
[‡] Foundation for Research and Technology-Hellas.
[§] University of Crete.

10.1021/jp8097999 CCC: $40.75
Published on Web 03/30/2009

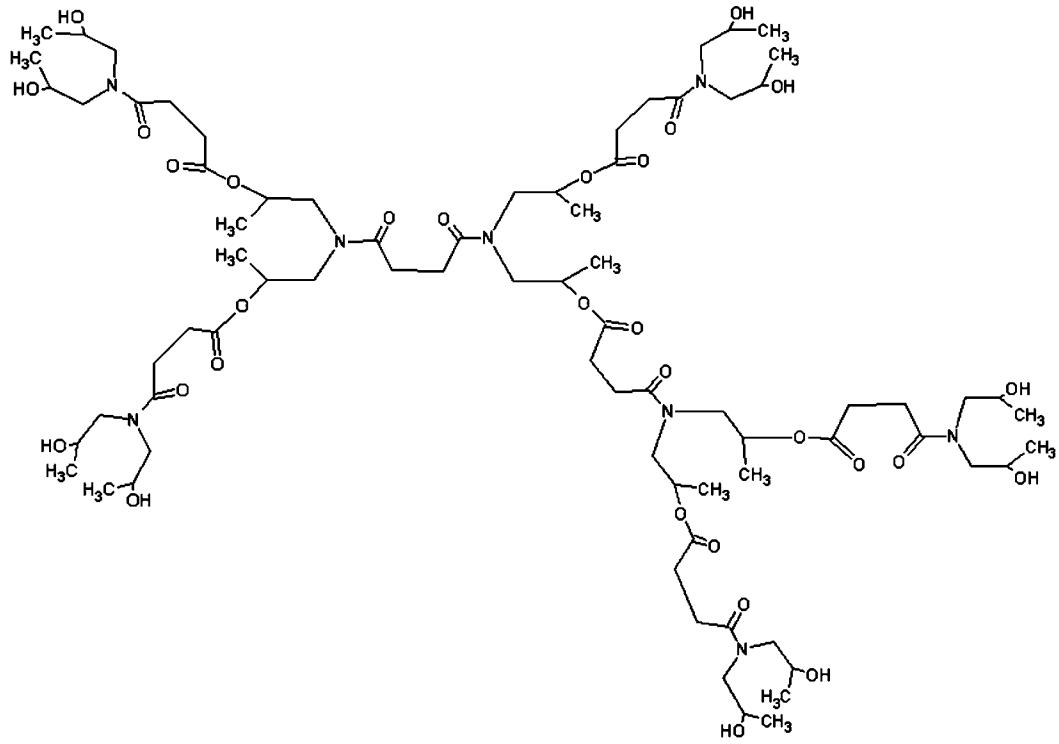

Figure 1. Chemical structure of the examined molecule.

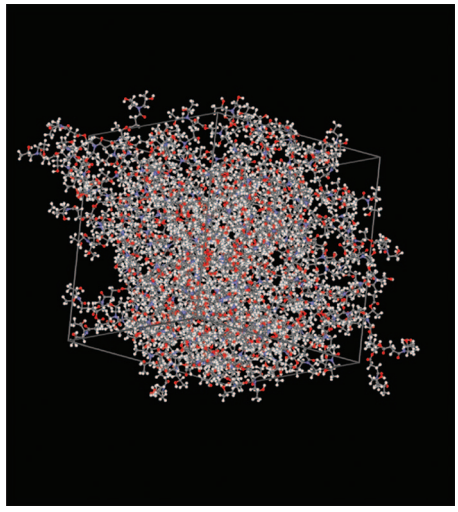

Figure 2. Snapshot of an equilibrated Hybrane melt at $T = 510$ K.

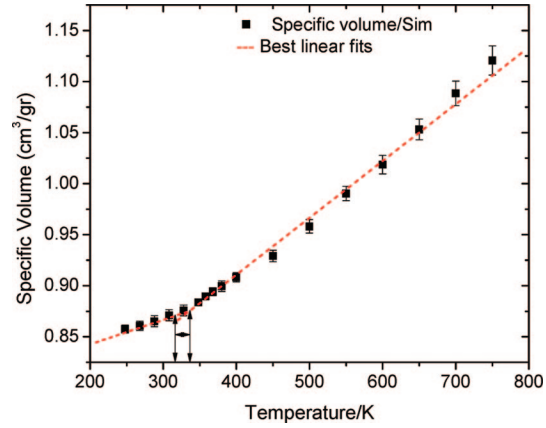

Figure 3. Specific volume as a function of temperature determined by the NPT simulation runs. Straight lines denote linear least-squares fits for the melt and the glass regions. The double arrows mark the temperature range, where a change in slope is detected due to the glass transition temperature.

equilibration) followed by 40 000 to 100 000 steepest-descent and conjugate gradient energy minimization cycles. Prior to production runs in the constant energy ensemble (NVE), 2−4 ns of further molecular dynamics runs in the isobaric−isothermal ensemble were performed, until standard equilibrium criteria were met regarding the energy (stabilized potential and total energy with small relative energy fluctuations), the thermodynamics (stable average of the specific volume), and the conformation of the molecules (stable average of radius of gyration). Figure 2 shows the structure obtained after application of the above-described equilibration protocol at $T = 510$ K.

Ensuing the equilibration steps, production trajectories of 2−8 ns (depending on the temperature) in the NVE ensemble (employing periodic boundary conditions) with a time step of 1 fs and frame-saving frequency of 1 ps were generated.[29] The size of the cubic simulation cell at NVE runs (as determined by the preceding NPT runs at each temperature) varied approximately between 47 and 50 Å.

Static and Structural Properties

The temperature dependence of the specific volume at the end of the NPT equilibration runs can be used in order to identify the glass transition temperature (T_g) of the Hybrane melt, as is shown in Figure 3.

The nominal glass transition temperature, T_g, as determined by the change in slope[30,31] was found to lie within 43 and 63 °C. Experimentally, the glass transition temperature of the studied Hybrane molecule was found[15] to be in the range of 40−50 °C (in that reference, the molecule corresponding to our study is referred to as H1200). Apart from the fact that the effective simulation "cooling rate" is much higher compared to a typical experimental one (10 K/min), other factors that could trigger deviations between the simulation and the experimental T_g value are the polydispersity of the actual molecules[32] as well as the possibility of the existence of traces of solvent used in

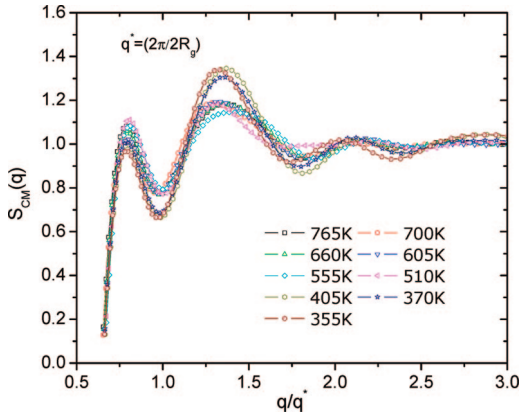

Figure 4. Static structure factor arising from the centers of mass of the molecules (shown for temperatures at which NVE runs were performed). The *x*-axis is normalized to the *q* value corresponding to an intermolecular separation of twice the radius of gyration.

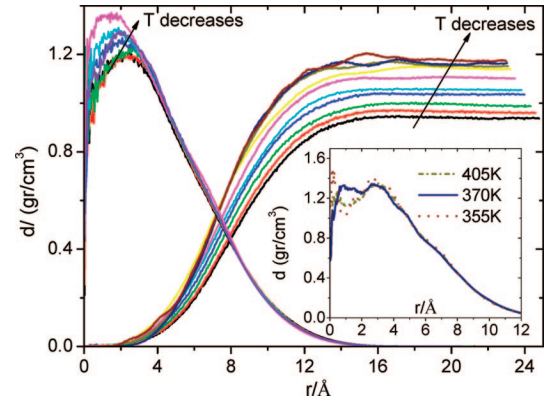

Figure 5. Density distributions with respect to the molecular center of mass, where the intra- and intermolecular contributions are shown separately. Arrows denote the direction of decreasing temperature. The temperatures range from 765 to 355 K as in Figure 4. The intramolecular distributions for temperatures 765−460 K are shown in the main panel whereas those for temperatures 405, 370, and 355 K are shown in the inset.

the synthesis procedure or traces of adsorbed water, which would lower the experimentally determined T_g.[33] Measurement of the density of the actual Hybrane sample supplied by DSM at ambient temperature (buoyancy method, ASTM D792) rendered a density of 1.18 g/cm^3 only about 2% higher compared to the value estimated from the simulation results.

The spatial arrangement of the Hybrane molecules in the melt was examined by evaluating the static structure factor arising from the centers of mass of the molecules according to eq 1

$$S_{CM}(q) = 1 + \frac{1}{N}\left\langle \sum_{i=1}^{N}\sum_{j\neq i}^{N} \frac{\sin(qr_{ij})}{qr_{ij}} \right\rangle \qquad (1)$$

where q refers to the magnitude of the scattering wave vector. N is the number of the molecules in the simulation box (here 40) while indices i,j correspond to different molecules. The angular brackets denote both ensemble and time averages.

Figure 4 shows the static structure factors determined by the above procedure at temperatures well above as well as close to the detected glass transition temperature. In all cases, the spectra exhibit a narrow maximum prior to the main peak. Taking as reference the magnitude of a scattering vector (q^*) corresponding to a center of mass separation of $2R_g$, the narrow maximum corresponds to approximately 25% larger distance. The appearance of this peak is consistent with a clustering mechanism between Hybrane molecules, much in analogy to the behavior characterizing associated colloidal[34] and hyperbranched[35] systems. The driving force for such an associative behavior between Hybrane molecules is most probably the hydrogen bond formation as found in other polymeric systems;[36] this will be discussed in detail later on in the present paper. The peaks appearing at larger q values indicate a liquidlike arrangement of the centers of mass over shorter distances; the main peak at $q/q^* \sim 1.4$ corresponds to the first neighbors at distances $\sim 1.4R_g$ (the radii of gyration ranged between 7.6 and 8.1 Å at the lowest and the highest examined temperatures, respectively).

To visualize the changes in density within an individual molecule, the distribution of density is constructed with respect to the molecular center of mass. The intra- and intermolecular contributions are shown separately in Figure 5. At high temperatures the intramolecular contribution assumes its larger value close to the center of mass exhibiting a gradual monotonic decrease near the periphery. In this temperature range (Figure 5, main panel), the intramolecular density profiles gradually become narrower assuming higher maximum values and shifting the location of their maximum to distances closer to the center of mass as the temperature decreases. Interpenetration from neighboring molecules becomes appreciable only at distances comparable to half the radius of gyration of the molecules. Upon decreasing temperature the degree of interpenetration (i.e., the degree of overlap between intra- and intermolecular distributions) grows, while the intermolecular profiles level off at values corresponding to the average system density at every temperature.

At low temperatures, however, characteristic changes take place. Distinct density areas apparently develop in the intramolecular density profiles, as indicated by the emergence of separate peaks at distances close to the center of mass (inset of Figure 5), while, on the other hand, the degree of interpenetration from neighboring molecules increases significantly. Such changes within the hyperbranched structure upon decreasing temperature are reminiscent of those observed in regular-branched dendrimer systems,[37,38] indicating the direct effect of the proximity to the glass transition region to the local packing in the atomic and the molecular scale. Note that this effect is observed even for the highest temperature in the inset, which is 70−90 K above the estimated T_g of our system (Figure 3).

Solubility Parameters

The miscibility of the studied molecules with other compounds is one of the key properties for a number of potential applications,[3,13] particularly for those where the hyperbranched structure is meant to be exploited in order to promote solubilization of otherwise insoluble moieties (e.g., drugs or other substances of biomedical interest).[15] Recent experiments[39] employing inverse gas chromatography (IGC) have provided relevant data for the partial solubility parameters at temperatures close to those examined in the present computational study. We have calculated the total as well as the partial solubility parameters arising from van der Waals, hydrogen-bonding, and polar interactions and compared them to the corresponding experimental values in order to check the ability of the present model to reproduce thermodynamic data that are particularly sensitive to the adopted energetic parameters and the relevant molecular conformations. The solubility parameters were estimated using the calculated values of the cohesive energy density[40,41]

$$\delta_k = \sqrt{\frac{E_{coh}^k}{V}} \quad (2)$$

Here E_{coh}^k represents the cohesive energy of intermolecular origin due to the kth energetic component (k = d, p, h for dispersive (d), polar (p), and hydrogen-bonding (h) energies) and V is the volume of the system. The different energy contributions were calculated as time averages from the trajectories of the equilibrated models. The total solubility parameter δ_{tot} is related to the partial parameters according to $\delta_{tot}^2 = \delta_d^2 + \delta_h^2 + \delta_p^2$, where δ_d, δ_h, and δ_p denote the partial solubility parameters arising from the respective energetic contributions. In our simulations no distinction has been made between dispersive and hydrogen-bonding contributions; therefore, these terms will be quoted by one parameter, δ_{dh}, which is related to the individual contributions as $\delta_{dh}^2 = \delta_d^2 + \delta_h^2$. Table 1 lists the total and the partial solubility parameters for two temperatures as determined experimentally[39] and as calculated from the present simulations.

Given the polydispersity of the actual sample and the sensitivity of the relevant calculations, the values from experiment and simulations agree well within the error margins, lending credibility to the adopted force field and the simulation procedure. As follows from the partial solubility parameters, the most significant contribution arises from the combined dispersive/hydrogen-bonding interactions.

In order to assess the role of intra- and intermolecular pair interactions, it is informative to obtain an estimation regarding their relative contributions. This information is valuable if, for instance, one wishes to quantify the effects of modifying either peripheral or internal polarizable groups to the solubilization properties of Hybrane-based systems. Figure 6 presents the number distribution of pairs separated at most by the van der Waals cutoff radius as a function of their distance from the center of mass of an individual molecule. The distance of each pair is defined as that between the center of mass of a Hybrane molecule and the atom of the pair, which is closer to the center of mass. The area under the curves is proportional to the number of the respective pairs. A direct visual inspection of the pair number profiles indicates that the intermolecular pairs contribute the most to the nonbonded dispersive energy (almost twice as much) compared to the intramolecular ones. The most probable distance of the intermolecular pairs from the center of mass is very close to the radius of gyration of the molecule (about 8 Å), while, for the intramolecular pairs, the peak of the distribution is shifted to a distance moderately closer to the center of mass. The shape of the intermolecular distributions remains effectively unchanged for high temperatures, while an asymmetry in the shape accompanied by a slight shift of the peak position toward smaller distances is observed for lower temperatures.

The observed shift is consistent with the enhanced degree of interpenetration between molecules, while the asymmetry in shape could be related to the development of spatial heterogeneities within the molecular structure upon approaching the glass transition, as indicated in Figure 5.

Hydrogen Bonding

Apart from contributing to the total solubility parameter via its contribution to the cohesive energy density, the formation of hydrogen bonds is one of the key mechanisms for the potential formation of complexes between hyperbranched polymers and other molecules[19,42] possessing appropriate groups (e.g., in applications involving blends/mixtures with surfactants or biological molecules), or the associative behavior observed in polymeric materials,[36] and, thus, important for the physicochemical behavior of such systems in different thermodynamic environments.[43] Hybrane possesses atoms which can act as donors or acceptors in hydrogen bond pairs, and the existence of hydrogen bonding has been verified by infrared (IR) spectroscopy experiments in the bulk through the shifts of the characteristic absorption bands of the carbonyl and hydroxyl groups.[33] It is, therefore, of interest to examine the extent of hydrogen bond formation both of intra- and intermolecular origin.

Along these lines, we have examined the radial distribution functions between characteristic donor−acceptor pairs, namely hydroxyl oxygen (OH)−hydroxyl hydrogen (HO), ester carbonyl oxygen (OS)−hydroxyl hydrogen (HO), and amide carbonyl oxygen (OA)−hydroxyl hydrogen (HO). To identify the peak associated with hydrogen-bond formation, we have utilized as criteria the characteristic hydrogen-acceptor distance and the angle φ formed by two electronegative atoms A, B and the hydrogen (i.e., the A−H−B angle). As documented in early studies,[44] genuine hydrogen-bond formation commonly requires that φ is larger than $\varphi_0 \approx 140°$, while in the majority of cases (including hydrogen bonds between carbonyl oxygens and hydrogen[45]) the H···O separation lies within 1.8−2.0 Å. To check the fulfillment of the above criteria, we have constructed radial distribution functions involving the aforementioned atomic pairs, taking into account only those pairs for which φ is larger than a specified value φ_0. Figure 7 shows such intra- and intermolecular functions at one temperature (T = 460 K) for one of the studied pairs (H−OA), at $\varphi > \varphi_0 = 0$ (all pairs are taken into account), $\varphi > \varphi_0 = 120°$, and $\varphi > \varphi_0 = 140°$ (the behavior at all other temperatures and for all the studied pairs is similar).

Apparently, the larger the φ_0 the more intense and the better separated the peak close to 2 Å distance becomes. On the grounds of the aforementioned criteria, we can attribute this maximum to hydrogen-bond formation. For the HO−OH pair (not shown here), the expected hydrogen-bond-related peak at ∼2 Å separation is discernible even at $\varphi_0 = 0°$ and it is significantly intensified as φ_0 increases as well. Since at $\varphi > 140°$ the H···O peak is well resolved for all the examined pairs, we will use $\varphi_0 = 140°$ for the presentation of all pair correlation functions, as well as for the determination of the range of separations over which the "hydrogen-bond" peak (HBP) extends, for all the examined pairs.

Figure 8 presents the temperature dependence of the pair correlation functions for the HO−OA and HO−OH pairs, resolved in intra- and intermolecular parts (the behavior for the HO−OS pair, not shown here, is analogous to that of OH−OA).

Focusing on the intramolecular curves (Figure 8a,c), it appears that the relative intensity characterizing HBP does not exhibit any systematic dependence on temperature for the HO−OH case, while for the HO−OA pair a trend toward an increasing intensity seems to describe the corresponding HBP behavior as the temperature decreases. In both cases, however, the HBP appears to be better resolved (note the lowering of the minima after the HBP) upon decreasing temperature. This effect can be attributed to the decrease of the kinetic energy of the atoms, which promotes the stability of the formed hydrogen bonds. However, a systematic increase of the HBP intensity can be observed in the intermolecular correlation functions (insets of Figure 8b,d) for both hydrogen-bonding pairs. This behavior is consistent with the increase of the degree of interpenetration

TABLE 1: Comparison of the Total and the Partial Solubility Parameters between Experiment[39] and Simulations from the Present Work[a]

temp (K)	experiment			simulation		
expt (sim)	δ_{tot} (MPa)$^{1/2}$	δ_{dh} (MPa)$^{1/2}$	δ_{p} (MPa)$^{1/2}$	δ_{tot} (MPa)$^{1/2}$	δ_{dh} (MPa)$^{1/2}$	δ_{p} (MPa)$^{1/2}$
368.1 (370)	15.16 ± 0.49	14.82 ± 1.3	3.32 ± 0.12	16.04 ± 1.22	15.48 ± 0.71	4.17 ± 2.09
358.1 (355)	15.67 ± 0.39	15.38 ± 1.2	2.99 ± 0.10	16.16 ± 1.21	15.79 ± 0.69	3.39 ± 2.50

[a] In the first column the simulation temperatures appear in parentheses.

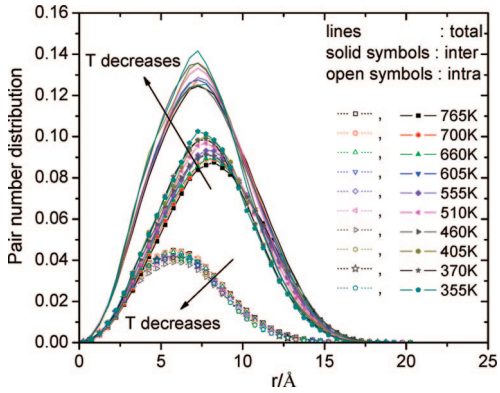

Figure 6. Number distributions of pairs contributing to the dispersive energy. Open and solid symbols represent intramolecular and intermolecular contributions, respectively, while lines correspond to the overall distributions.

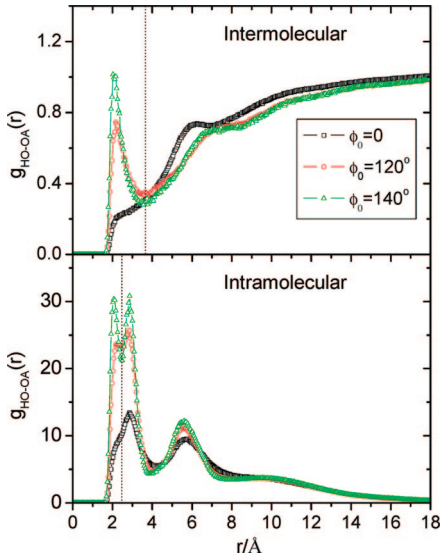

Figure 7. Inter- (upper panel) and intramolecular (lower panel) correlation functions of the hydroxyl hydrogen (HO) and amide carbonyl oxygen (OA) pairs at different φ_0 angles (see text) at T = 460 K. The vertical dotted lines denote the maximum separation at which the HO−OA pairs are considered to form a hydrogen bond.

between the Hybrane molecules upon densification of the system, which, in turn, increases the probability of closer contacts between intermolecular donor−acceptor atoms.

At constant temperature, a rough estimate regarding the relative probability of hydrogen-bond formation between the examined atomic species can be made by comparing the relative intensities of the respective HBP's appearing in the pair correlation functions. Figure 9 illustrates such a comparison for the intra- and intermolecular cases at one temperature (T = 460 K).

The observed behavior is representative for the other temperatures as well. Comparing the relative intensities of the hydrogen bonds involving carbonyl oxygens for the intramolecular case, it seems that formation of HO-OS hydrogen bonds is more favorable compared to the HO-OA pair, despite the fact that the number of OA sites per molecule (8) is larger than the one of OS (6) (see Figure 1). The intensity of the HO-OH intramolecular HBP is comparable to that corresponding to the HO-OS analogue. On the other hand, the relative probability of formation of intermolecular hydrogen bonds is comparable among the examined pairs. The picture emerging from Figure 9 provides a fair description over the entire temperature range.

In order to explore a dynamic aspect associated with hydrogen bonding, we have calculated a survival time correlation function defined as,[46]

$$P(t) = \frac{\sum_{(i,j)} p_{ij}(t)}{\sum_{(i,j)} p_{ij}(t=0)} \tag{3}$$

where $p_{ij}(t)$ takes the value of 1 if the hydrogen bond that exists between the ith and the jth atoms at $t = 0$ survives at time $t > 0$ and 0 otherwise. The summation runs over all the atomic pairs, which are found to form a hydrogen bond at $t = 0$. Due to the subpicosecond time scales anticipated for hydrogen-bond lifetimes,[47,48] we have specifically generated trajectories with a frame-saving frequency of 2 fs, so that we can explore the dynamics of hydrogen-bonding behavior at a wider temporal window. The obtained dynamic functions were analyzed by determining the distribution of exponential relaxation times (DRT).[49,50] According to this method, a dynamic function is considered as a continuous superposition of single exponential processes: $C(t) = \int_{-\infty}^{\infty} F(\ln(\tau))\ e^{-t/\tau}\ d\ \ln\ \tau$, where F is the obtained DRT. Relaxation times corresponding to different dynamic mechanisms (appearing as different peaks in the distribution) are estimated via the first moment of the calculated distribution function $F(\ln(\tau))$ over the pertinent time range. If the entire time window is taken into account, an overall average relaxation time equivalent to integrating the dynamic function can be calculated instead. For dynamic processes represented by symmetric peaks in the distribution, the time location of the corresponding peak provides a good estimation of the characteristic relaxation time.

Figure 10 presents the hydrogen-bonding survival correlation functions (eq 3) as a function of temperature, arising from intra- (Figure 10a) and intermolecular (Figure 10c) HO−OH pairs, together with the corresponding distributions of relaxation times (Figure 10, b and d, respectively). Focusing on the intramolecular pairs (Figure 10a), it may clearly be discerned either from the survival functions themselves (note the two-step decay) or from the corresponding distributions (existence of two peaks) that two very different time scales characterize the HO−OH intramolecular hydrogen-bonding dynamics. The longest one, described by the slower of the two processes (Figure 10b), is of the order of hundreds to thousands of picoseconds (as implied by the location of the corresponding maxima) and depends strongly on temperature (the lower the temperature the longer

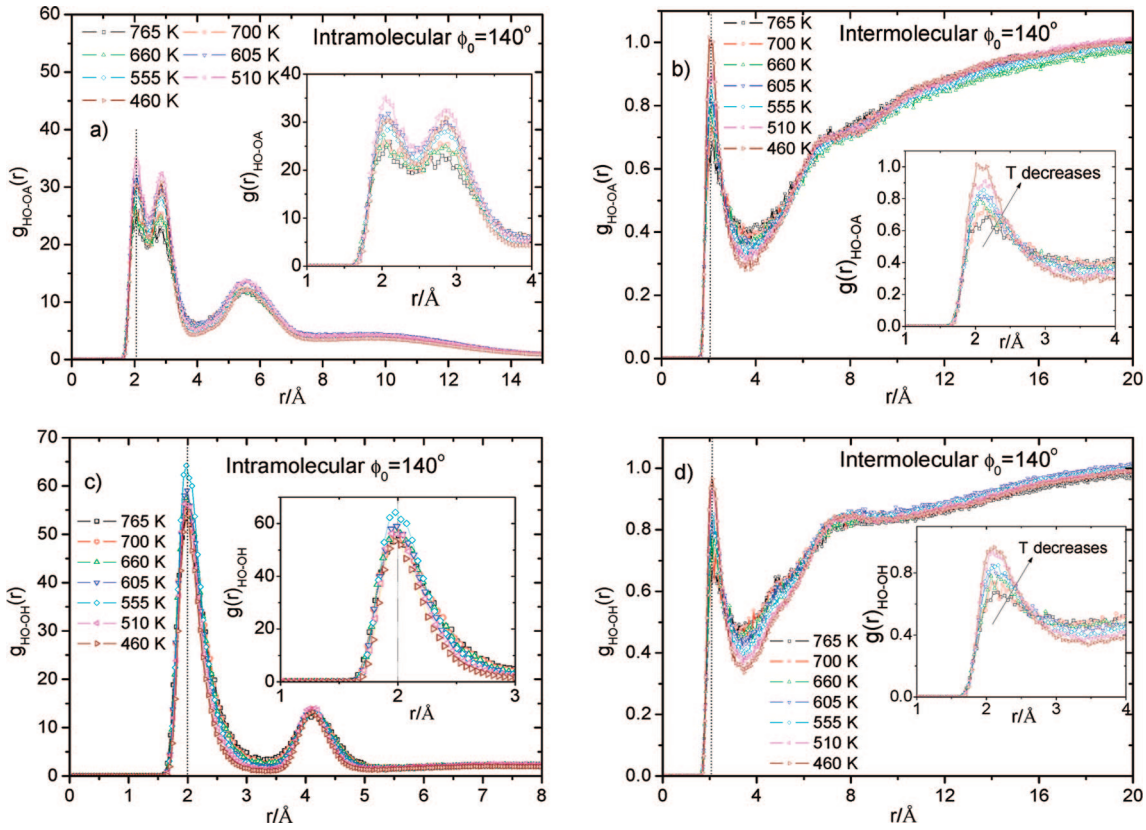

Figure 8. Temperature dependence of the OH−OA (a, b) and OH−HO (c, d) pair correlation functions at $\varphi_0 = 140°$, separated into the intra- (a, c)and intermolecular (b, d) contributions. The dotted vertical lines denote the location of the peak due to hydrogen-bond formation. Insets show a magnification of the corresponding main graphs in the range of distances over which the "hydrogen-bond" peak extends.

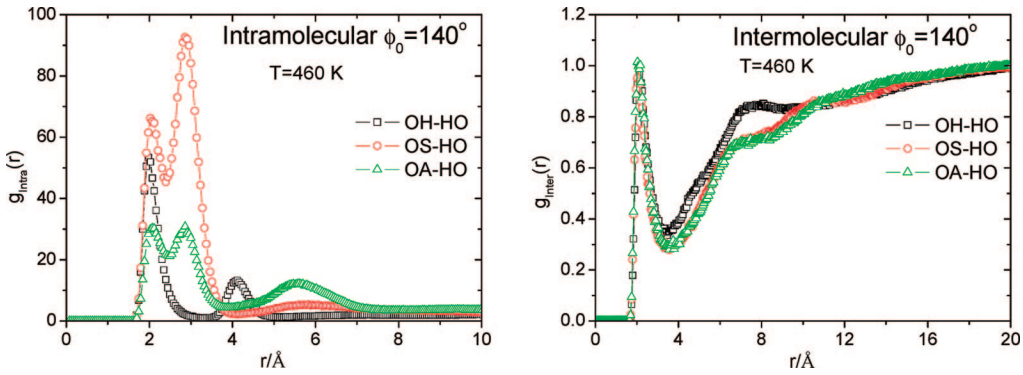

Figure 9. Comparison of the intra- (left) and intermolecular (right) contributions of the examined pair correlation functions at constant temperature $T = 460$ K.

the characteristic time). The short time scale is of the order of 10 fs, and the corresponding peak presents features (position of maxima and width) practically unaffected by the temperature changes in the examined temperature range. The considerably higher amplitude (i.e., area under the peak) of the faster process compared to that of the slower one indicates that this is the principal mechanism via which hydrogen-bonding dynamics is realized for the examined donor−acceptor pair. The intermolecular spectra (Figure 10d) are characterized by a single process at a time scale of ∼10 fs (similarly to the fast intramolecular one) with a temperature-insensitive width and time scale. The principal disparity in the behavior of the intramolecular OH−OH pair (Figure 10a,b) with that describing the intermolecular hydrogen-bond analogues (Figure 10c,d) is the effective absence of a long time scale mechanism as implied by the vanishing amplitude of the peak at the long time scale regime (Figure 10d). The fast relaxation process exhibits features similar to those characterizing the corresponding intramolecular peak indicating a common underlying mechanism.

Figure 11 presents plots analogous to those of Figure 10 but for the HO−OS hydrogen-bond pair. A description similar to that of the HO−OH pairs applies for the case of HO−OS analogues, for both the intra- and intermolecular pairs. The behavior of the HO−OA pairs is in complete analogy as well. From a direct visual inspection, a notable difference between the two sets is the considerably higher amplitude of the slower process in the HO−OH intramolecular pair (Figure 10b) compared to its HO−OS one (Figure 11b). This implies that the mechanism related to the slow process is much more significant for the HO−OH pairs in the long-time limit.

To follow the temperature dependence of the two time scales appearing in the hydrogen-bonding time survival spectra, we have calculated the times corresponding to the two peaks appearing in the respective DRTs and constructed the Arrhenius

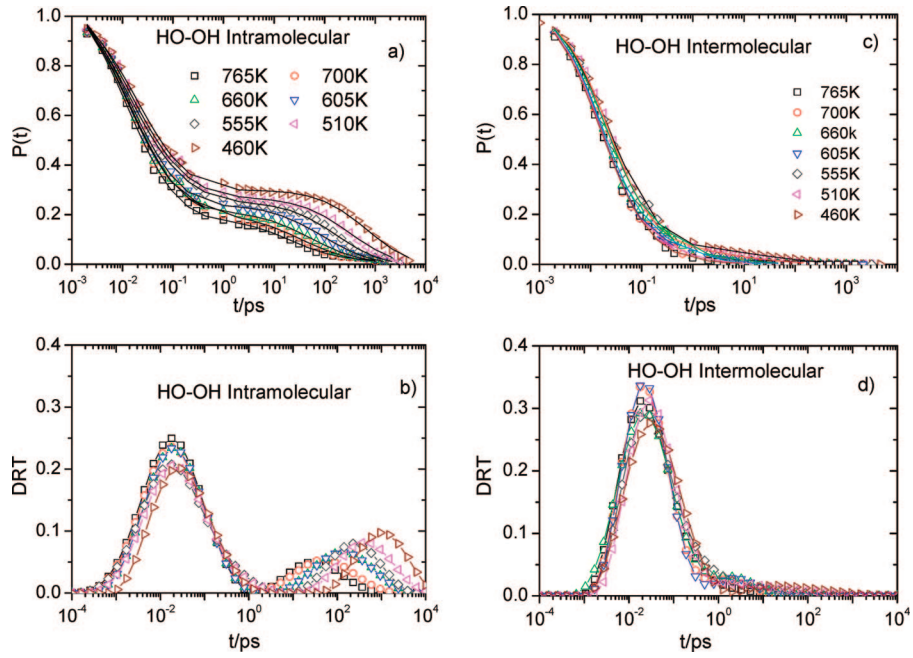

Figure 10. Combined high (2 fs) and lower resolution (1 ps) survival time correlation functions for the HO−OH pairs arising from hydrogen bonds of intra- (a) and intermolecular (c) origin. The lines through the points denote the fits resulting from the DRT analysis. Lower panels (b,d) show the corresponding time distribution functions. Only temperatures at which complete decorrelation is reached are shown.

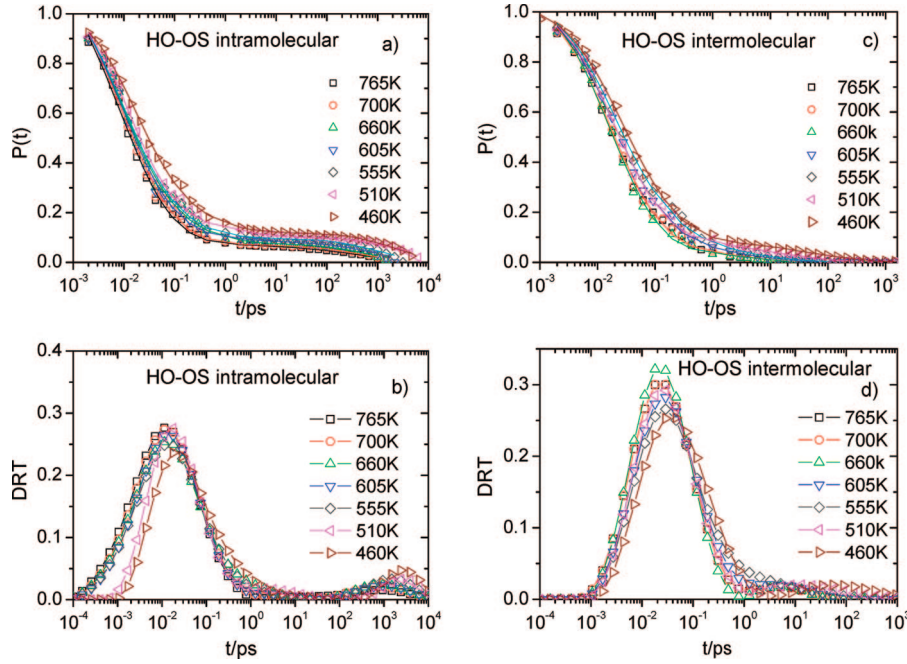

Figure 11. Combined high (2 fs) and lower resolution (1 ps) survival time correlation functions for the HO−OS pairs arising from hydrogen bonds of intra- (a) and intermolecular (c) origin. The lines through the points denote the fits resulting from the DRT analysis. Lower panels (b,d) show the corresponding time distribution functions. Only temperatures at which complete decorrelation is reached are shown.

plot shown in Figure 12. The abbreviations appearing in the legend are as follows: A stands for intra, E for inter, F for fast, and S for slow. Therefore, for example A-S means intraslow, E-F means interfast, and so on. The rates (inverse times) of the fast process lie within the same range for all the examined pairs and exhibit a very weak temperature dependence. On the other hand, the slow process of the HO−OH intramolecular pair shows a stronger temperature dependence (its time scale increases upon decreasing temperature). The rates corresponding to the slow process of the HO−OA and HO−OS pairs appear to follow a very weak temperature dependence as well, but this can be attributed to the rather low amplitude of the associated process (see Figure 11b), which introduces a large uncertainty in the analysis.

The fit of the data to the Arrhenius equation results in an activation energy for the fast process of 5.1 ± 1.1 kJ/mol while a fit to the slow HO−OH process yields a value of 12.1 ± 0.2 kJ/mol. Due to the definition of the relevant pair correlation function, the calculated activation energies may deviate from the characteristic energy of a hydrogen bond as extracted, e.g., from spectroscopic experiments; however, the so-calculated activation energy of the fast process, which corresponds to a time scale close to the expected hydrogen-bond lifetimes,[47,48] lies within the range characterizing normal-to-weak hydrogen

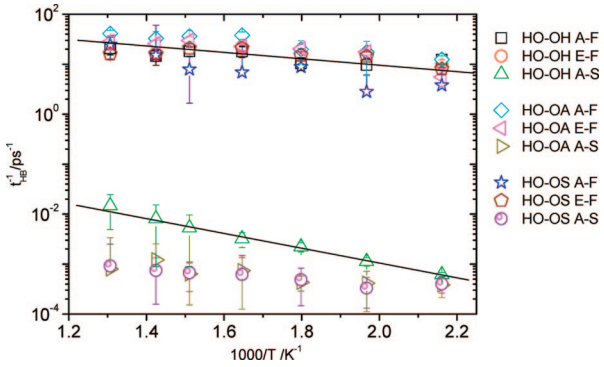

Figure 12. Relaxation rates calculated from the DRT analysis for the slow (S) and the fast (F) processes appearing in the intramolecular (A) and intermolecular (E) distributions arising from the relevant survival time correlation functions as a function of inverse temperature. Lines represent least-squares fits to the Arrhenius equation. For the abbreviations appearing in the legend, see text.

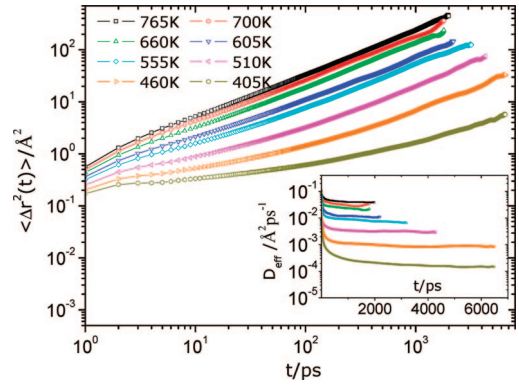

Figure 13. Main panel: mean-squared displacement of the centers of mass for different temperatures (only temperatures at which diffusional behavior was attained within the simulation window are shown). Inset: effective diffusivities extracted form the mean-squared displacement data as a function of time. The curves from top to bottom correspond to the temperatures shown in the main panel, in descending order. The attainment of a plateau at long times signifies the long-range diffusional behavior.

bonds.[51] The larger activation energy of the slow HO−OH mode combined with its longer relaxation time imply a possible connection to a more sluggish long length scale motion.

To understand the physical origins of the two processes appearing in the hydrogen-bonded pairs, we can compare the spectral features characterizing the respective peaks in the distributions and the related relaxation times. The very short time scale of the fast process and its constant amplitude in the high temperature regime are consistent with a hydrogen-bond formation/breaking process.[47] The slowing down observed at low temperatures could be related to the overall slowing down of the system as it approaches the glass transition (e.g., via the slowing down of the motion of the covalent bonds in which the donor and the acceptor participate). Since the slow process is present in the dynamics of intramolecular pairs and is absent in that of the intermolecular pairs, it should be related to a motional process of intramolecular nature and, thus, to the internal dynamics of an individual molecule. Light into the origin of the slow process in the intramolecular pairs can be shed by the apparent temperature dependence of its characteristic times (based on the behavior of the OH−OH data, for which one can be highly confident); the temperature dependence is a key feature of polymer dynamics at the segmental or the entire molecule scale.[52] The relation of the slow process to time scales characterizing internal dynamics of the examined molecule will be discussed below following the detailed examination of the motional mechanisms of Hybrane described in the next section. Such a coupling between conformational transitions of a polymer and hydrogen-bonding alteration dynamics has already been observed experimentally in polymer complexes.[53]

Local and Global Molecular Dynamics

Dynamic properties associated with the polymeric nature of Hybrane were examined both over the local and over the entire molecule scale by means of appropriate time correlation functions (TCF). In particular, TCF's describing the rotational motion in both local and global scales as well as the shape/size fluctuations were calculated. In addition to the calculation of TCF's, the diffusive molecular motion was monitored by following the mean-squared displacement of the center of mass. For validation purposes, results of the temperature dependence of relevant relaxation times were compared to data from rheological measurements of the actual polymer provided by DSM.

A. Translational Motion. The translational motion of the molecules in the bulk was probed by calculating the mean-squared displacement (MSD) of the center of mass as shown in Figure 13. As expected, a slowing down of the overall motion is observed as the temperature decreases. At lower temperatures (still well above T_g), a subdiffusional behavior at intermediate time scales develops, analogous to the one observed in previous studies of linear[54] or hyperbranched polymers;[38] this subdiffusional motion is the precursor of the plateau region associated to the "caging" of molecules due to the kinetic arrest prior to the diffusional motion, near to the glass transition temperature.[38,54]

Diffusional behavior is attained at long times for these temperatures as can be seen in the inset of Figure 13, where the effective diffusivities extracted from the MSD data of the center of mass are shown as a function of time for the temperatures of Figure 13. The effective diffusivities are calculated according to

$$D_{\mathrm{eff}}(t) = \frac{\langle \Delta r^2(t) \rangle}{6t} = \frac{1}{6t}\langle |\mathbf{R}_{\mathrm{cm}}(t) - \mathbf{R}_{\mathrm{cm}}(0)|^2 \rangle \qquad (4a)$$

where $\mathbf{R}_{\mathrm{cm}}(t)$ is the center of mass vector at time t. The angular brackets denote ensemble average over the 40 molecules considered, while multiple time origins have been used in the averaging. The long-range diffusion coefficients are extracted from the plateau values of D_{eff} at long-times:

$$D_{\mathrm{cm}} = \lim_{t \to \infty} D_{\mathrm{eff}}(t) \qquad (4b)$$

The temperature dependence of the diffusion coefficient is evident from the decrease in the plateau values upon lowering the temperature, in the inset of Figure 13.

B. Size and Shape Fluctuations and Global Rotational Motion. The dynamics of size and shape fluctuations can be probed via the time correlation of the fluctuations of the squared radius of gyration (R_g)[55]

$$C_{R_g}(t) = \frac{\langle R_g^{\,2}(0) R_g^{\,2}(t) \rangle - \langle R_g^{\,2} \rangle^2}{\langle R_g^{\,4} \rangle - \langle R_g^{\,2} \rangle^2} \qquad (5)$$

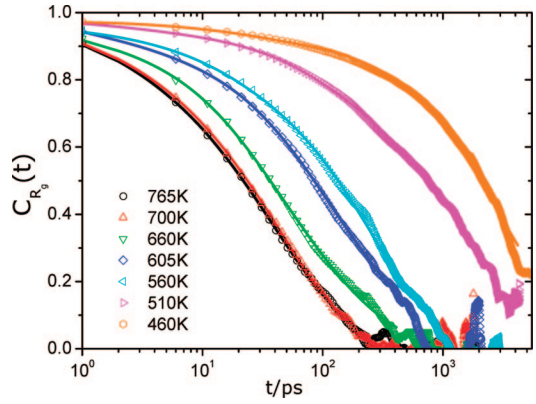

Figure 14. Radius of gyration correlation functions (eq 6) at different temperatures. The lines through the points represent the fits resulting from the DRT analysis quoted earlier.

where $R_g = (1/N)\sum_{i=1}^{N} \langle|\mathbf{r}_i - \mathbf{R}_{cm}|^2\rangle$. N is the number of all atoms of the molecule, $\mathbf{r}_i$ is the position vector of the ith atom and $\mathbf{R}_{cm}$ the center of mass vector. The correlation function described by eq 5 provides information regarding the characteristic time of the "breathing" motion of the molecule.

Figure 14 depicts $C_{R_g}(t)$ at different temperatures. As was noted for the translational motion as well, a decrease in temperature results in a retardation of the overall fluctuating motion of the molecule (note the decay of $C_{R_g}(t)$ at longer time scales as temperature drops) from hundreds of picoseconds to nanoseconds. Analysis following the DRT method provides a good fit to the spectra as indicated by the lines through the data points.

Because of the nature of the dynamic process described by C_{R_g}, it is not uncommon, particularly in the case of hyperbranched molecules[56] and even more in the bulk state, where any long length-scale motion requires the cooperative movement of the neighboring molecules, that coupling with other global motional mechanisms takes place. To check whether this holds true in the case of Hybrane, we have also examined the dynamics of the overall rotational motion of the molecule. This can be probed, e.g., by calculating the second-order Legendre polynomial

$$G_2(t) = \frac{1}{2}\langle 3[\hat{\mathbf{h}}(t)\cdot\hat{\mathbf{h}}(0)]^2 - 1\rangle \qquad (6)$$

of unit vectors $\hat{\mathbf{h}}$, which connect the center of mass of each molecule with the individual atoms. Such a correlation function essentially relaxes via the reorientational motion of the entire molecule.[57]

Figure 15 displays the $G_2(t)$ spectra at different temperatures, together with the corresponding fits (solid lines through the data points) and the respective DRT's resulting from the applied analysis. The slowdown of the overall rotational motion upon decreasing temperature is evident from the shift of the $G_2(t)$ curves to longer times. This retardation of the molecular reorientation upon lowering the temperature can be visualized by the analogous shift of the location of the main (slower) process of the time distribution spectra.

Actually the increase of the width of the slow process upon decreasing temperature is particularly evident. A broader peak denotes a larger dispersion in the characteristic times of the elementary exponential processes, indicative of a more dynamically heterogeneous environment.[54,58] The increasing dynamic heterogeneity is directly linked to the proximity to the glass

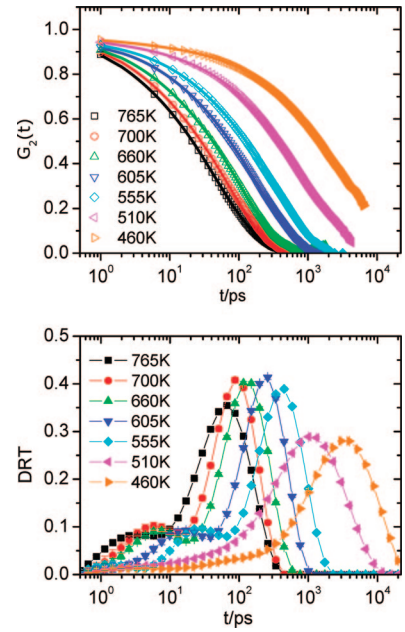

Figure 15. Upper panel: global reorientational correlation functions with the respective fits (solid lines through the points). Lower panel: corresponding distributions of relaxation times.

transition.[38,54] The lower amplitude peak appearing in the DRT spectra at much shorter time scales can be attributed to shorter-length-scale motions[55,57] of the order of a few bonds, which relax prior to the complete decorrelation of the overall rotational motion.

It should be noted here that the observed orientational relaxation spectra cannot be accounted for by simple Rouse or reptation-like theories applied to linear polymer melts (for a brief discussion, see Appendix B). Since the dynamic mechanism described by $G_2(t)$ relates to the entire molecular scale as does the "breathing" motion of the molecule, both of these processes are expected to be closely associated with each other as conjectured earlier. Moreover, they should be related to the rheological response of the material since they essentially represent the longest dynamic time scales of the molecule.

To check whether we can corroborate this notion experimentally, we have performed zero-shear viscosity (η_0) measurements on the bulk Hybrane sample, which at low shear rates is expected to follow the same temperature dependence as that of the longest relaxation time of the polymer,[59,60] and compared it with the temperature dependence of the average relaxation times obtained from the G_2 and the C_{R_g} correlation functions (Figures 14 and 15). Details on the rheological experiments and on the procedure to obtain the temperature dependence of the zero-shear viscosity are provided in Appendix A.

Figure 16 shows the average relaxation times corresponding to the distribution spectra from Figures 14 and 15 plotted together with a line that corresponds to the temperature dependence of the Vogel−Fulcher−Tamman expression obtained from the analysis of the experimental data of the zero shear viscosity (see Appendix A). In doing so, we have applied eq 7

$$\tau = \tau_0 \exp\left(\frac{B}{T - T_0}\right) \qquad (7)$$

keeping the parameters B and T_0 the same as those describing the η_0 data (Figure 20, Appendix A), and allowing only the

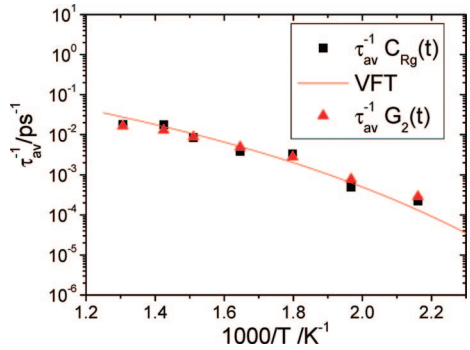

Figure 16. Average relaxation times (points) corresponding to the C_{R_g} and G_2 spectra of Figures 14 and 15, respectively, together with a VFT curve using the B and T_0 parameters which describe the zero shear viscosity behavior (Figure 20, Appendix A). The value of τ_0 obtained from the present fit is 0.7 ps. The error bars are comparable to the size of the symbols.

variation of the prefactor τ_0, i.e., performing a shift by a constant in the (logarithmic) y-axis.

A first observation is that the size/shape fluctuations and the overall rotation of the molecule (points in Figure 16) are realized practically at the same time scale within the examined temperature range, attesting to the coupling between these two kinds of motional mechanisms in the bulk. Moreover, to a good approximation their temperature dependence follows that of the experimental zero shear viscosity of the actual material. The latter finding is consistent to the anticipated connection between the longest relaxation time of the molecule and its macroscopic viscosity, providing at the same time a strong support for the adequacy of the current simulations in reproducing the physical behavior of the examined system.

C. Local Orientational Motion. The dynamics at a local length scale can be probed by calculating the time correlation function of the reorientation of selected bonds, $C(t)$

$$C(t) = \frac{1}{2}\langle 3[\hat{\mathbf{k}}(t)\cdot\hat{\mathbf{k}}(0)]^2 - 1\rangle \qquad (8)$$

of unit vectors $\hat{\mathbf{k}}$, which lie along the examined bond. We have monitored the C−C and the HO-OH bonds as representative ones, since they are located either on the outer branch or in the interior of the molecular structure (see Figure 1).

Figure 17 displays the orientational correlation functions for the C−C bonds together with the corresponding DRT's. At the higher examined temperatures, only one broad relaxation process (peak) can be discerned at very short times (of the order of 1 ps). As the temperature decreases, however, the spectra appear to "split" to a very fast process with a temperature independent relaxation time (i.e., peak location), and to a slower process, which exhibits a characteristic time that depends strongly on temperature. At sufficiently high temperatures, the dynamics on the segmental scale (involving cooperative motion of several bonds) can be very fast exhibiting, thus, a time scale close to the individual bond reorientation. However, as the segmental motion involves a more extended part of the molecule than a single bond, it requires the synergistic motion of the immediate bonded and nonbonded neighbors for its realization; this requirement introduces a dynamic heterogeneity in the local relaxation times, which is reflected on the width of the respective distributions.[61]

At lower temperatures, the segmental dynamics becomes much slower compared to the rapid tumbling bond motion,

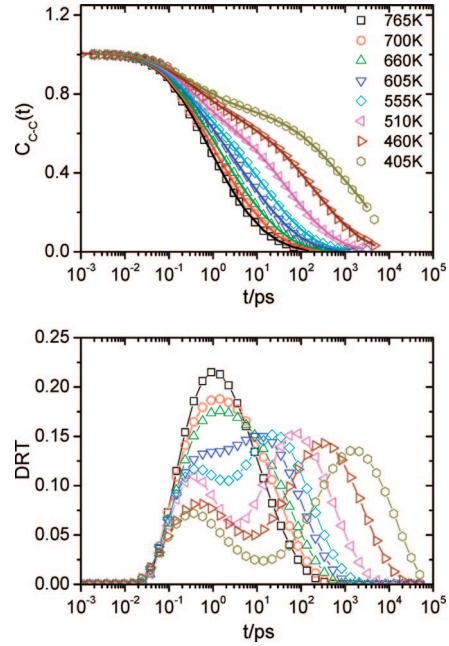

Figure 17. Upper panel: reorientational correlation function for the C−C bond in between the carbonyl carbons (see Figure 1). Lower panel: corresponding distribution of relaxation times.

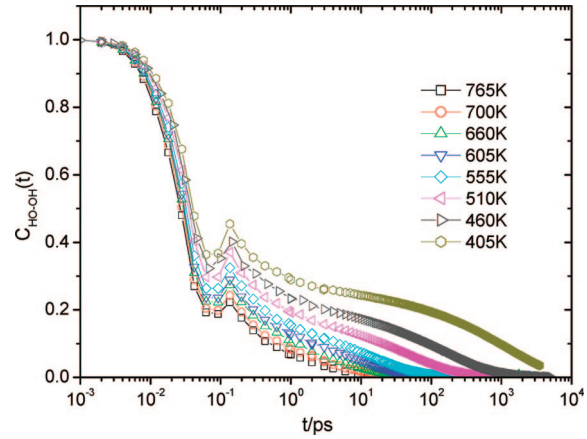

Figure 18. Orientational correlation functions (eq 8) for hydroxyl oxygen−hydroxyl hydrogen bonds.

leading to the separation of the two time scales. This separation is manifested in the distributions as the "split" of the high-temperature broad peak, to a temperature-independent fast process with low amplitude and to a slower mode of high amplitude that exhibits a strongly temperature-dependent characteristic time. The higher amplitude of the slower mode at low temperatures indicates that the segmental motion that involves the branch on which the examined C−C bond resides in (see Figure 1) becomes the principal channel via which the bond reorientation relaxes. The increasing slowing-down of its time scale alludes to the gradual freezing-in of even the local conformational motions as the glass transition is approached.

Figure 18 shows the orientational correlation functions of the hydroxyl O−H bonds. Similarly to the case of the C−C bonds, the spectra exhibit a fast process at a subpicosecond time scale (note the fast drop of the correlation function to a decorrelation degree of more than 60%) and a slower process with a temperature-dependent time scale (evident by the shift of the terminal decay to longer times as the temperature decreases).

An additional characteristic of the O−H bond spectra, not observed in the C−C bond dynamics, is an apparent recorre-

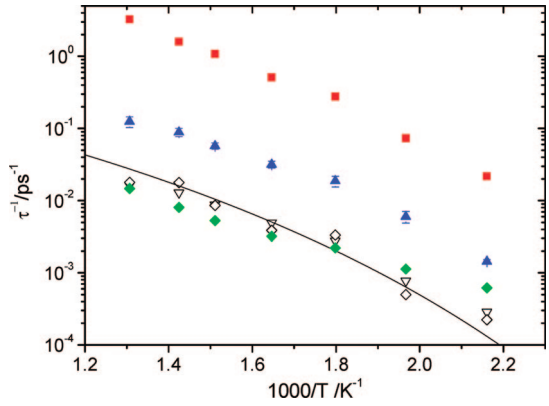

Figure 19. Average relaxation rates (inverse relaxation times) both for global (overall molecule rotation, ▽, molecular size/shape fluctuations, ◇) and local (bond reorientation) motions for the HO−OH (■) and the C−C (▲) bonds. The points assigned to hydrogen bonding (HO−OH intra, ◆) correspond to the characteristic time of the slow process from the hydrogen-bond survival correlation function, which also appear in Figure 12. The times referring to H−O reorientation were calculated by integrating the respective correlation functions. The solid line denotes the VFT behavior from Figure 16.

lation (i.e., an increase of the value of the correlation function) at a time scale of ∼0.2 ps. The slower process can be attributed to the segmental motion as discussed above for the C−C bond. Similarly, the faster process can be ascribed to the fast tumbling motion of the H−O bond. The fact that the time scales associated with the fast process in the H−O bond spectra appear shorter compared to the analogous modes observed in the C−C bond dynamics (compare the respective time scales at which the correlations functions in Figures 17 and 18 exhibit their initial drop) can be attributed to the larger degree of motional "freedom" of the H−O since hydroxyls are located at the "free-ends" of the molecule (Figure 1). In view of the time location at which the recorrelation at the H−O bond reorientation appears and the fact that an analogous effect is not observed in the C−C bond spectra, one can assign its origin to the dynamic formation/breaking of the hydrogen bonds, which is realized exactly at that specific time scale (see the times for the fast process in Figure 12).

Figure 19 shows the temperature dependence of the bond relaxation rates ($1/\tau$), together with the ones corresponding to motions on the scale of the entire molecule and the slow process detected in the HO−OH intramolecular hydrogen-bond pair. As anticipated from the hierarchy of polymer dynamics, bond relaxation rates are the fastest compared to the other motions. Among them, the OH−HO bond reorientational motion relaxes at shorter times due to the large contribution of the faster process (Figure 18) in the average relaxation time. The slow process associated with the HO−OH intramolecular hydrogen bonding is realized at a time scale very close to that of the molecular "breathing" motion, which is consistent with the picture described earlier regarding its origin. It should be emphasized that both local (as expressed mainly by the C−C bond reorientation) and global dynamics apparently follow the same temperature dependence, which characterizes the macroscopic viscosity of the actual material as well, as discussed above in relation to Figure 16.

Summary and Conclusions

Molecular dynamics simulations have been utilized to investigate the static and dynamic behavior of a characteristic hyperbranched molecule of the poly(ester amide) family, Hybrane. A fully atomistic representation was adopted in order to obtain a better insight to its structure−properties relation by examining its behavior in the bulk over a wide temperature range covering temperatures far above as well as close to the experimental glass transition temperature.

The model used provides a reasonable description of experimental data obtained from calorimetric (glass transition temperature), chromatographic (solubility parameters by means of inverse gas chromatography) and rheological (temperature dependence of the macroscopic viscosity) measurements. Based on this level of agreement with experiment and on the detail afforded by the atomistic nature of the simulations, the static and dynamic properties were explored over different length and time scales, including the examination of certain hydrogen-bonding capabilities of the molecule.

Upon decreasing temperature, the degree of interpenetration between neighboring molecules increases while spatial heterogeneities develop close to the center of mass of the molecules. The resulting close intermolecular contacts near the molecule periphery are found to contribute almost twice as much to the energetics associated with the solubility behavior of the system compared to the intramolecular ones. This information could be exploited when control of the solubility properties of similar hyperbranched systems (e.g., with different functional groups or with different number of peripheral units) is desired.

Regarding the hydrogen-bonding capabilities of Hybrane, it was found that both, intra- and intermolecular donor−acceptor pairs participate in hydrogen bonding. As a general rule, the probability of hydrogen-bond formation increases upon decreasing temperature. Between the examined hydrogen-bond-capable pairs, a larger probability for the formation of intramolecular HO−OH hydrogen bonds was found, while among donor−acceptor pairs involving carbonyl oxygens, it was found that formation of hydrogen bonds by the ester carbonyl oxygen was more favorable. The principal mechanism associated with hydrogen-bond formation/breaking between donor−acceptor pairs was found to be realized at a very short time scale (of the order of 0.01−0.1 ps depending on temperature) for both the intra- and the intermolecular pairs. However, an additional process with times longer by several orders of magnitude and a rather strong temperature dependence was observed in the behavior of the intramolecular pairs. Based on the time scale and on the fact that the slow process appears only in intramolecular pairs (Figures 10 and 11), it seems plausible to associate its origin with the internal dynamics of the molecule. Comparison between the time scale of this slow process and the one corresponding to the size/shape fluctuations ("breathing") of the molecule (Figure 19) supports the latter argument. This finding implies that the conformational properties of the examined molecule can play a significant role to the observed hydrogen-bonding behavior.

The internal "breathing" motion of the molecule appears to be coupled to its overall rotation (Figures 16 and 19). The time scale describing these motions essentially corresponds to the maximum molecular relaxation time and appears to follow to a good approximation the temperature dependence of the experimentally determined macroscopic zero-shear viscosity (Figures 16 and 19). Similar temperature dependence seems to be followed by the dynamics on the length scale of a bond, particularly for bonds located near the interior of the molecule (Figure 19). To this extent, the simulation results indicate that Hybrane behaves as a thermorheologically simple polymer.[52]

Several of the structural features characterizing Hybrane (branching, existence of hydrogen-bond-forming groups in the

interior and in the periphery, absence of entanglements and capability of interpenetration) are commonly met in a wide range of hyperbranched polymers (e.g., poly(amido amines), poly(propylene amines), polyesters, etc.). It is therefore believed that the mechanisms discussed in the present work may serve as a basis for the description of a broader class of systems, particularly those that exhibit features similar to Hybrane, which render them water soluble and capable of complex formation via hydrogen bonding.

Acknowledgment. Part of this research was sponsored by the Greek General Secretariat for Research and Technology under the framework of the PENED 2003 program (grants 03EΔ716, 03EΔ581) and by NATO Scientific Affairs Division (Science for Stability Programme). The authors thank T. Goudoulas and G. Dalakoglou for assistance in the rheological measurements.

Appendix A

The rheological measurements were performed using an AR-G2 stress-controlled rheometer (TA Instruments) in the parallel plate geometry and in the linear viscoelastic regime, at a constant frequency $\omega = 1$ Hz and for a wide temperature range above the glass transition temperature, T_g. The obtained zero-shear viscosity data are shown in Figure 20 together with a fit according to the commonly used Vogel−Fulcher−Tamman (VFT) function[60]

$$\eta_0 = \eta_{0,0} \exp\left(\frac{B}{T - T_0}\right) \qquad \text{(A.1)}$$

In the latter expression $\eta_{0,0}$ is a prefactor, T_0 is the so-called Vogel temperature, which is lower than the actual T_g by an additive constant, while B can be considered as a material constant. Evidently, the VFT expression provides an excellent fit to the temperature dependence of the zero shear viscosity.

Appendix B

As it has been noted in previous studies regarding the calculation of the relaxation spectra of nonregular hyperbranched molecules,[62,63] their complex topological details impart significant differences with respect to the behavior observed in linear polymers. To demonstrate that, we have calculated the end-to-end vector correlation function according to the Rouse model for polymer melts (no entanglement effects are expected in low molecular weight hyperbranched molecules[64]), which is the closest analogue to the orientational correlation function as can be probed by vectors $\hat{\mathbf{h}}$ (eq 6). Figure 21 illustrates the comparison of the first-order orientational correlation function $G_1(t) = \hat{\mathbf{h}}(t)\cdot\hat{\mathbf{h}}(0)$ with the normalized end-to-end vector autocorrelation function, $P(t)$, of an equivalent (in terms of size and diffusion coefficient) linear polymer according to the Rouse model.[64] The diffusion coefficients (plateau values in Figure 13, inset) and the radii of gyration as calculated from our simulations were used in the construction of $P(t)$. That is, we have assumed the validity of the relations $D_{cm} = k_B T/N\zeta$ and $\langle R_g^2 \rangle \cong Nb^2/6$, where N is the number of statistical segments, b the statistical segment length, and ζ the monomeric friction coefficient.

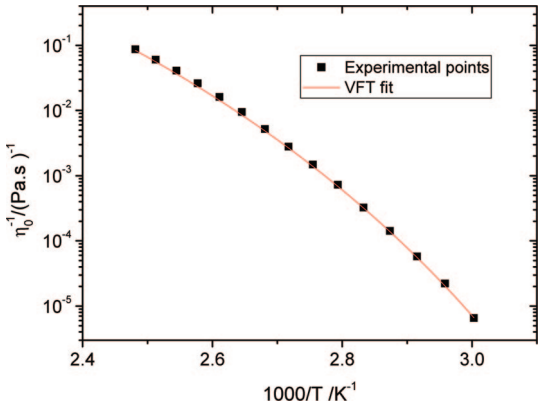

Figure 20. Temperature dependence of the experimental zero shear viscosity. The line represents the best fit according to the VFT expression. The parameters providing the best fit are $\eta_{0,0} = 3.75 \times 10^{-5}$ Pa·s, $B = 2079.23$ K, $T_0 = 239.0$ K.

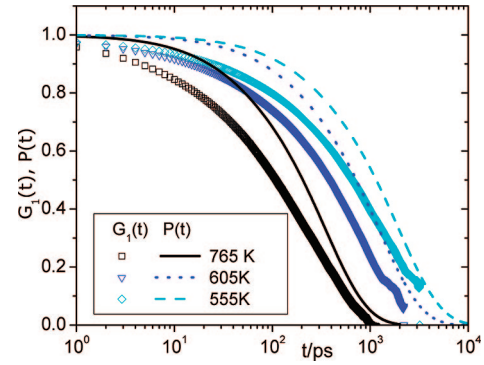

Figure 21. Comparison of the first-order orientational correlation function $G_1(t)$ to $P(t)$ (see text) for three temperatures. In the calculation of $P(t)$ only the modes $p = 1$ and $p = 3$ were considered.

As shown, the simulation spectra deviate systematically from those that would correspond to an analogous "Rouse" linear polymer melt. A detailed comparison between the simulation spectra and existent more specific theories is left for a future study.

References and Notes

(1) Gao, C.; Yan, D. *Prog. Polym. Sci.* **2004**, *29*, 183.
(2) Voit, B. I. *C. R. Chim.* **2003**, *6*, 821.
(3) Holmes, M. *Plastics, Additives Compounding* **1999**, *1*, 18.
(4) Sun, M. H.; Bo, Z. S. *J. Polym. Sci., Polym. Chem.* **2007**, *45*, 111.
(5) Yates, C. R.; Hayes, W. *Eur. Polym. J.* **2004**, *40*, 1257.
(6) Korolev, G.; Bubnova, M. *Polym. Sci. Ser. C* **2007**, *49*, 332.
(7) Muscat, D.; van Benthem, R. A. T. M. *Top. Curr. Chem.* **2001**, *212*, 41.
(8) Gelade, E. T. F.; Goderis, B.; de Koster, C. G.; Meijerink, N.; van Benthem, R.; Fokkens, R.; Nibbering, N. M. M.; Mortensen, K. *Macromolecules* **2001**, *34*, 3552.
(9) Froehling, P. E. *J. Polym. Sci. Part A: Polym. Chem.* **2004**, *42*, 3110.
(10) Lebib, A.; Natali, M.; Li, S. P.; Cambril, E.; Manin, L.; Chen, Y.; Janssen, H. M.; Sijbesma, R. P. *Microelectron. Eng.* **2001**, *57−8*, 411.
(11) Lebib, A.; Chen, Y.; Cambril, E.; Youinou, P.; Studer, V.; Natali, M.; Pepin, A.; Janssen, H. M.; Sijbesma, R. P. *Microelectron. Eng.* **2002**, *61−62*, 371.
(12) Natali, M.; Lebib, A.; Cambril, E.; Chen, Y.; Prejbeanu, I. L.; Ounadjela, K. *J. Vac. Sci. Technol. B* **2001**, *19*, 2779.
(13) Wågbergb, L.; Ondaral, S.; Enarsson, L.-E. *Ind. Eng. Chem. Res.* **2007**, *46*, 2212.
(14) Ondaral, S.; Wågbergb, L.; Enarsson, L.-E. *J. Colloid Interface Sci.* **2006**, *301*, 32.
(15) Suttiruengwong, S.; Rolker, J.; Smirnova, I.; Arlt, W.; Seiler, M.; Luederitz, L.; de Diego, Y. P.; Jansens, P. J. *Pharm. Dev. Technol.* **2006**, *11*, 55.
(16) Froehling, P.; Brackman, J. *Macromol. Symp.* **2000**, *151*, 581.
(17) Zhang, S. H.; Jin, X.; Painter, P. C.; Runt, J. *Polymer* **2004**, *45*, 3933.
(18) Sui, Z. J.; Jaber, J. A.; Schlenoff, J. B. *Macromolecules* **2006**, *39*, 8145.
(19) Fernandez, L.; Gonzalez, M.; Cerecetto, H.; Santo, M.; Silber, J. *J. Supramol. Chem.* **2006**, *18*, 633.

(20) Cheng, Y. Y.; Xu, T. W. *Eur. J. Med. Chem.* **2005**, *40*, 1188.
(21) Lehn, J.-M. *Rep. Prog. Phys.* **2004**, 249.
(22) Accelrys. Cerius 2 Package.
(23) Wang, J.; Cieplak, P.; Kollman, P. A. *J. Comput. Chem.* **2000**, *21*, 1049.
(24) Posocco, P.; Ferrone, M.; Fermeglia, M.; Pricl, S. *Macromolecules* **2007**, *40*, 2257.
(25) Lee, H.; Baker, J. R.; Larson, R. G. *J. Phys. Chem. B* **2006**, *110*, 4014.
(26) Gasteiger, J.; Marsili, M. *Tetrahedron* **1980**, *36*, 3219.
(27) Allen, M.; Tildesley, D. *Computer Simulation of Liquids*; Oxford Science Publications: New York, 1997.
(28) Weiner, S. J.; Kollman, P. A.; Nguyen, D. T.; Case, D. A. *J. Comput. Chem.* **1986**, *7*, 230.
(29) Forester, T.; Smith, W. CCLRC, Daresbury Laboratory, Daresbury, Warrington Wa4 4AD, England. The simulations were performed by utilization of an appropriately modified version of the DL_POLY package. DL_POLY is a parallel molecular dynamics package developed at Daresbury laboratory, and is a property of the Council for the Central Laboratory of the Research Councils (CCLRC).
(30) McKenna, G. In *Comprehensive Polymer Science*; Pergamon Press: Oxford, UK, 1989; Vol. 2.
(31) Han, J.; Gee, R. H.; Boyd, R. H. *Macromolecules* **1994**, *27*, 7781.
(32) DSM; www.hybrane.com.
(33) Lüderitz, L. Influence of the structure of hyperbranched polymers on the release kinetics of pharmaceuticals. M.Sc. Thesis, Technische Universitaet Berlin, 2004.
(34) Haw, M. D.; Poon, W. C. K.; Pusey, P. N. *Physica A* **1994**, *208*, 8.
(35) Karatasos, K. *Macromolecules* **2008**, *41*, 1025.
(36) *Hydrogen Bonded Polymers*; Binder, W., Ed.; Springer: Heidelberg, Germany, 2007.
(37) Karatasos, K. *Macromolecules* **2006**, *39*, 4619.
(38) Karatasos, K.; Lyulin, A. V. *J. Chem. Phys.* **2006**, *125*, 184907.
(39) Dritsas, G. S.; Karatasos, K.; Panayiotou, C. *J. Polym. Sci. Part B: Polym. Phys.* **2008**, *46*, 2166.
(40) Jena, K. K.; Raju, K. V. S. N.; Prathab, B.; Aminabhavi, T. M. *J. Phys. Chem. B* **2007**, *111*, 8801.
(41) Hansen, C. M. *J. Paint Technol.* **1967**, *39*, 104.
(42) Kleinman, M. H.; Flory, J. H.; Tomalia, D. A.; Turro, N. J. *J. Phys. Chem. B* **2000**, *104*, 11472.
(43) He, Y.; Zhu, B.; Inoue, Y. *Prog. Polym. Sci.* **2004**, *29*, 1021.
(44) Speakman, J. C. *The hydrogen bond and other intermolecular forces*; The Chemical Society: London, 1975.
(45) Lommerse, J. P. M.; Price, S. L.; Taylor, R. *J. Comput. Chem.* **1997**, *18*, 757.
(46) Swiatla-Wojcik, D. *Chem. Phys.* **2007**, *342*, 260.
(47) Tamai, Y.; Tanaka, H.; Nakanishi, K. *Macromolecules* **1996**, *29*, 6761.
(48) Texeira, J.; Luzar, A.; Longeville, S. *J. Phys.: Condens. Matter* **2006**, *18*, s2353.
(49) Provencher, S. *Comput. Phys. Commun.* **1982**, *27*, 229.
(50) Provencher, S. A general-purpose constrained regularization method for inverting photon correlation data. In *Photon Correlation Techniques in Fluid Mechanics*; Schulz-DuBois, E. O., Ed.; Springer-Verlag: Berlin, 1983.
(51) Geffrey, G. A.; Saenger, W. *Hydrogen bonding in biological structures*; Springer-Verlag: Heilderberg, Germany, 1991.
(52) Strobl, G. *The physics of polymers*, 2nd ed.; Spinger-Verlag: Berlin, 2007.
(53) Miyoshi, T.; Takegoshi, K.; Terao, T. *Macromolecules* **1999**, *32*, 8914.
(54) Baschnagel, J.; Varnik, F. *J. Phys: Condens. Matter* **2005**, *17*, R851.
(55) Dalakoglou, G. K.; Karatasos, K.; Lyulin, S. V.; Lyulin, A. V. *J. Chem. Phys.* **2007**, *127*, 214903.
(56) Dalakoglou, G. K.; Karatasos, K.; Lyulin, S.; Lyulin, A. *J. Chem. Phys.* **2008**, *129*, 034901.
(57) Karatasos, K.; Adolf, D. B.; Davies, G. R. *J. Chem. Phys.* **2001**, *115*, 5310.
(58) Karatasos, K. *Macromolecules* **2005**, *38*, 4472.
(59) Rubinstein, M.; Colby, R. H. *Polymer Physics*; Oxford University Press: Oxford, UK, 2003.
(60) Ferry, J. D. *Viscoelastic properties of polymers*; Wiley: New York, 1980.
(61) Ediger, M. D. *Annu. Rev. Phys. Chem.* **2000**, *51*, 99.
(62) Jasch, F.; von Ferber, C.; Blumen, A. *Phys. Rev. E* **2003**, *68*, 051106.
(63) Gurtovenko, A. A.; Blumen, A. *Adv. Polym. Sci.* **2005**, *182*, 171.
(64) Doi, M.; Edwards, S. F. *The Theory of Polymer Dynamics*; Oxford University Press: Oxford, UK, 1986.

JP8097999